ORIGINAL ARTICLE

Inhalable nanoparticles with enhanced cuproptosis and cGAS−STING activation for synergistic lung metastasis immunotherapy

Chongzheng Yan[a,b], Huaiyou Lv[a,b,c], Yafei Feng[a,b], Yuhan Li[a,b], Zhongxi Zhao[a,b,*]

[a]Department of Pharmaceutics, Key Laboratory of Chemical Biology of Ministry of Education, School of Pharmaceutical Sciences, Cheelloo College of Medicine, Shandong University, Jinan 250012, China
[b]Key University Laboratory of Pharmaceutics & Drug Delivery Systems of Shandong Province, School of Pharmaceutical Sciences, Cheeloo College of Medicine, Shandong University, Jinan 250012, China
[c]Department of Pharmacy, Yantai Yuhuangding Hospital Affiliated to Qingdao University, Yantai 264001, China

Abstract   Due to the insufficient Cu^+ accumulation, Cu^+ efflux mechanism, and highly immunosuppressive tumor microenvironment (TME) in lung metastasis, the cuproptosis efficacy is limited. Herein, an inhalable nanodevice (CLDCu) is constructed to successfully overcome the drawbacks of cuproptosis. CLDCu consists of a Cu^{2+}-chitosan shell and low molecular weight heparin-tocopherol succinate (LMWH-TOS, LT) core with disulfiram (DSF) loading. The prepared CLDCu can be inhaled and accumulate in large amounts in lung lesions (63.6%) with 56.5 times higher than intravenous injection. Within tumor cells, the mild acidity triggers the co-release of DSF and Cu^{2+}, thus generating bis(diethyldithiocarbamate)-copper (CuET) to block Cu^+ efflux protein ATP7B and forming toxic Cu^+, leading to enhanced cuproptosis. Meanwhile, the released chitosan cooperates with CLDCu-induced cuproptosis to activate stimulator of interferon genes (STING) pathway, which significantly potentiates dendritic cells (DCs) maturation, as wells as evokes innate and adaptive immunity. In lung metastatic mice model, CLDCu is found to induce cuproptosis and reverse the immunosuppressive TME by inhalation administration. Moreover, CLDCu combined with

*Corresponding author.
    E-mail address: zxzhao@sdu.edu.cn (Zhongxi Zhao).

anti-programmed cell death protein ligand-1 antibody (aPD-L1) provokes stronger antitumor immunity. Therefore, nanomedicine that combines cuproptosis with STING activation is a novel strategy for tumor immunotherapy.

1. Introduction

Lung cancer is one of the most common malignancies worldwide, accounting for 20% of all cancer-related deaths[1,2]. Moreover, tumors at other sites can remodel the lung microenvironment to promote the invasion and metastasis of tumor cells, thereby producing metastatic tumors in the lungs[3−5]. It is estimated that 20%−54% of malignant tumors develop lung metastasis, which seriously threatens the survival and quality of life of patients[6,7]. In the course of clinical treatment, surgery, chemotherapy, and radiotherapy are used to treat lung metastasis[8−10]. Despite advances in these therapeutic strategies, the lung metastasis is mostly incurable, and 5-year survival rates of lung metastatic cancer is low[11]. Therefore, these traditional therapy modalities are still less than ideal for lung metastasis. Recently, a unique Cu^+-dependent death pathway that occurs by a new mechanism, termed "cuproptosis" has been discovered for the first time[12]. Cuproptosis relies heavily on intracellular Cu^+ accumulation and differs from all other known pathways[13]. Moreover, Cu^+ is more important for cuproptosis than Cu^{2+}, because Cu^+ can directly combine with lipoylated dihydrolipoamide S-acetyltransferase (Lip-DLAT) to increase DLAT oligomers levels and decrease Fe−S cluster proteins, thereby effectively triggering cuproptosis[14]. The mechanism of cuproptosis may invigorate research exploiting the unique role of Cu^+ to treat cancers. However, insufficient Cu^+ accumulation in tumor tissues, Cu^+ transporter ATP7B[15,16], and highly immunosuppressive tumor microenvironment (TME) undermine cuproptosis therapeutic efficacy. Therefore, it may be feasible to achieve enhanced cuproptosis-mediated lung metastasis therapy by designing new nanomedicines that simultaneously deliver large amounts of Cu^+, block Cu^+ efflux protein ATP7B, and reshape the tumor immune microenvironment (TIME) at lung metastatic sites.

Up to now, a variety of Cu^{2+} ionophores have been explored, such as elesclomol, pyrithione, and disulfiram (DSF)[12]. In contrast with other Cu^{2+} ionophores, DSF can react with Cu^{2+} to produce Cu^+[17,18], thus leading to more effective cuproptosis. Furthermore, DSF chelates with Cu^{2+} to generate bis(diethyldithiocarbamate)−copper (CuET), which displays more efficient reactive oxygen species (ROS) generation ability to inhibit ATP production and down-regulate Cu^+ transporter ATP7B expression[19], and then causes elevated levels of intracellular Cu^+, yielding a more intense cuproptosis-based therapy. Therefore, the co-delivery of sufficient DSF and Cu^{2+} to lung metastatic tissues by a reasonably efficient delivery system is absolutely a reasonable means to fully utilize Cu^+-induced cell death for lung metastasis therapy. The inhalation administration system exhibited increased drug accumulation in lung sites, thus presenting a potential treatment route for lung metastasis treatment[20,21]. However, due to rapid clearance by the mucociliary clearance mechanism, inhaled free DSF and Cu^{2+} show limited antitumor efficacy[22]. According to research, chitosan, a biodegradability and biocompatibility natural copolymer,

can achieve mucosal penetration and long-term retention in lungs[23]. Therefore, inhalation administration of DSF, Cu^{2+}, and chitosan offers ample potential to induce lung metastasis cuproptosis.

However, lung metastasis cannot be cured by cuproptosis treatment alone. Therefore, it has been proposed to combine cuproptosis with pyroptosis, ferroptosis, and immunotherapy to improve anti-metastatic efficacy[24−26]. In particular, cuproptosis can act as the immunogenic cell death (ICD) evoker to release damage-associated molecular patterns (DAMPs), and then improve tumor immunogenicity[24,25]. Despite the fact that cuproptosis combined with immunotherapy have shown some benefit for lung metastasis, cuproptosis-induced ICD still fails to induce enough antitumor immunity[27,28]. Emerging research suggests that chitosan can act as the adjuvant to activate cyclic-di-GMP-AMP synthase-stimulator of interferon genes (cGAS−STING) pathway, which stimulates DCs maturation and promotes $CD8^+$ T cells activation to initiate robust antitumor immune responses[29,30]. In addition, chitosan contains amino and hydroxyl groups that provide natural anchoring sites for Cu^{2+}[31]. Therefore, a novel inhalable nanoformulation based on the combination of DSF, Cu^{2+}, and chitosan, with enhanced cuproptosis and cGAS−STING activation, can be used for combined cuproptosis immune antitumor therapy.

Herein, we constructed an inhalable nanodevice with enhanced cuproptosis and cGAS−STING activation for effective lung metastasis immunotherapy, defined as CLDCu (C stands for chitosan, L for LMWH-TOS, D refers to DSF, and Cu is the symbol of Cu^{2+}). The CLDCu consisted of a Cu^{2+}-chitosan shell and low molecular weight heparin-tocopherol succinate (LMWH-TOS, LT) core with DSF loading (Fig. 1A). CLDCu administered by inhalation route can achieve increased Cu^{2+} and DSF accumulation in lung tissues. The Cu^{2+}-chitosan shell enabled efficient internalization by tumor cells. Following entering tumor cells, CLDCu would release Cu^{2+} and DSF under mildly acidic pH condition. Subsequently, the released DSF in situ chelated free Cu^{2+} to form CuET and convert Cu^{2+} into Cu^+, which could directly bind to Lip-DLAT aggregation and destabilize Fe−S cluster proteins. In addition, CuET could decrease intracellular ATP contents and then down-regulate Cu^+ efflux protein ATP7B expression. The synergistic effects could significantly trigger tumor cells cuproptosis and then restore tumor antigen recognition. Meanwhile, the released chitosan in combination with CLDCu-mediated cuproptosis strongly activated the cGAS−STING pathway, which stimulated DCs maturation and promoted immune activation within the tumor. In vivo experiments showed that inhalation of CLDCu could simultaneously elicit robust anti-metastatic response and convert the immunosuppressive TME to an immune-activating type. Moreover, the combination of inhalation of CLDCu and aPD-L1 could provoke more powerful antitumor immunity (Fig. 1B). Taken together, the
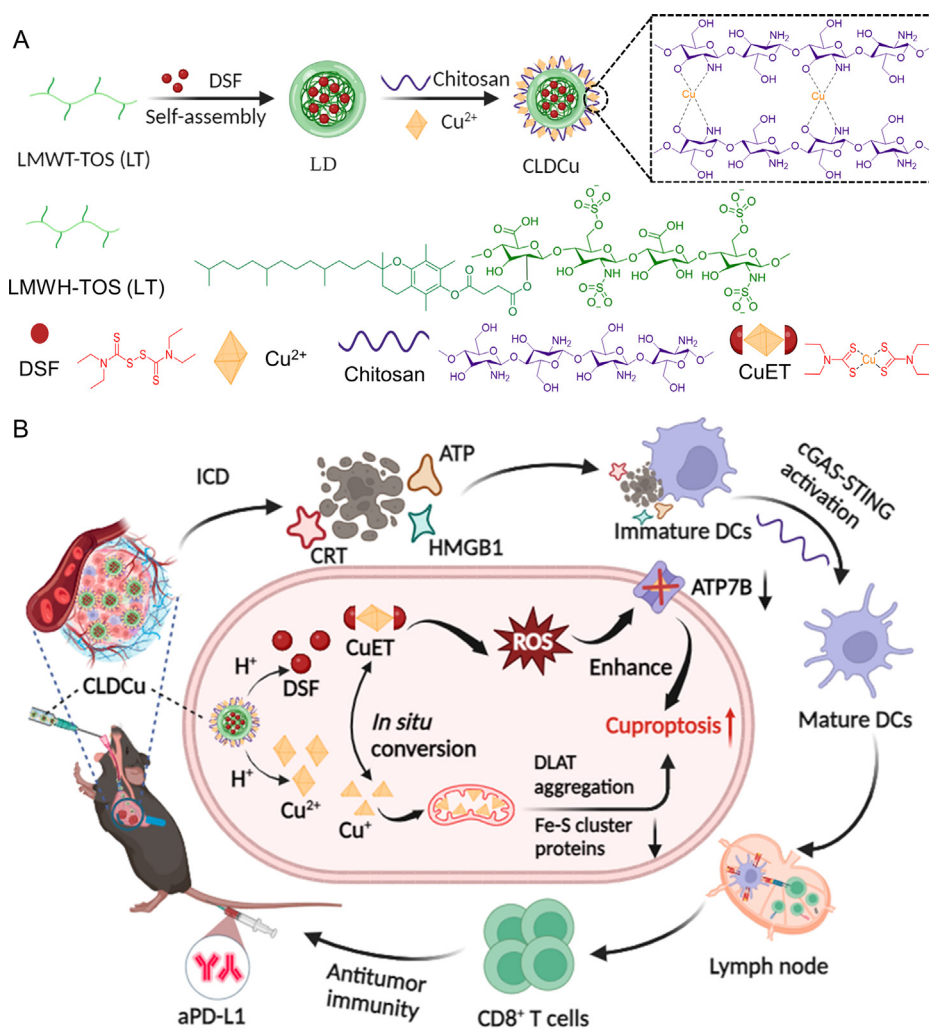
Figure 1 Inhalable CLDCu with amplified cuproptosis and cGAS−STING activation for enhanced lung metastasis immunotherapy. (A) Synthesis process of CLDCu. (B) Schematic illustration of CLDCu for amplified cuproptosis synergized immunotherapy *in vivo*.

successful construction of CLDCu sets an example to augment cuproptosis and activate cGAS−STING pathway for lung metastasis immunotherapy.

2. Materials and methods

2.1. Materials

Chitosan and disulfiram were purchased from Bide Pharmatech Ltd. (Shanghai, China). Coumarin 6 (C6), Cy5, reactive oxygen species (ROS) detection kit, ATP7B polyclonal antibody (AF6264), p-TBK1 polyclonal antibody (AF5959), and p-IRF3 polyclonal antibody (AF5848) were obtained from Beyotime Biotechnology (Shanghai, China). aPD-L1 antibodies (cat. no. BE0101) used for *in vivo* therapy were purchased from BioXCell Biotech Co. (New Hampshire, USA). GAPDH monoclonal antibody (60004-1-Ig), CRT monoclonal antibody (10292-1-AP), and DLAT polyclonal antibody (13426-1-AP) were obtained from Proteintech Group, Inc. (Rosemont, IL, USA). Lipoic acid (ab58724) and FDX1 (ab108257) were ordered from Abcam Ltd. (Shanghai, China). p-STING (Ser366) polyclonal antibody (PA5-105674) was acquired from Thermo Fisher Scientific Inc. (Massachusetts, USA). B16F10 cells and human umbilical vein endothelial cells (HUVECs) were obtained from the Chinese

Academy of Science Cells Bank (Shanghai, China). Six weeks old female C57BL/6J mice were obtained from Beijing Vital River Laboratory Animal Technology Co., Ltd. (Beijing, China). Animal experiments were approved by the Laboratory Animal Ethical and Welfare Committee of Cheeloo College of Medicine of Shandong University (ethical approval number: ECSPSSDU2023-2-227).

2.2. Methods

2.2.1. Preparation and characterization of CLDCu

Firstly, LMWH-TOS (LT) was synthesized following previous research[32]. Subsequently, CLDCu was synthesized by a "two-step" strategy. Specifically, LD was prepared following the emulsion-evaporation method[32]. Specifically, DSF (1.0 mg) dissolved in $CHCl_3$ (3 mL) and stirred for 30 min at 25 °C. Next, LT (10.0 mg) was mixed with the above DSF solution. Distilled water (3 mL) was added and sonicated to obtain a more homogenized solution. The LD (L for LMWH-TOS and D refers to DSF) powder was obtained after lyophilization for 24 h. Secondly, the chitosan solution (5 mg/mL, 1 mL) and the following $CuCl_3 \cdot 2H_2O$ solution (2.5 mg/mL, 1 mL) were immediately added under vortex. Finally, the solution pH was adjusted to about 7.4 to obtain CLDCu. The obtained CLDCu nanodevices were

centrifuged at 12,000 rpm (Z36HK, HermLe, GRE) for 30 min. The C6-CLCu and Cy5-CLCu were similarly synthesized.

2.2.2.   pH-triggered Cu^{2+} release from CLDCu

First, CLDCu (1 mg/mL, 1 mL) was incubated in PBS (pH 7.4, 6.8, and 5.5) at 37 °C. At predetermined time intervals (0.5, 1, 1.5, 2, 3, 4, 6, 8, 16, and 24 h), 200 µL of particle solution was taken out and centrifuged at 12,000 rpm (HermLe) for 30 min. The release efficiency of Cu^{2+} in the supernatants was measured by inductively coupled plasma mass spectra (ICP-MS).

2.2.3.   Determination of the ability of CLDCu to generate hydroxyl radical ($\cdot OH$)

·OH generation was investigated by using TMB as a probe[33]. The reaction was performed in the pH 5.5 PBS buffer containing 0.5 mmol/L TMB and 8 mmol/L H_2O_2. After respective incubation with DSF, CLCu, and CLDCu at pre-designed time points including 1, 5, 10, 15, 30, 45, 60, 90, 120, 180, 240, and 300 min oxTMB was monitored at the absorbance of 652 nm.

2.2.4.   Cellular uptake efficacy

To observe the cellular uptake in vitro, the coumarin 6 (C6, green) molecules instead of DSF were loaded in nanoparticles, named C6-L and C6-CLCu, respectively. B16F10 cells were seeded on confocal dishes (3×10^5 cells). C6-L and C6-CLCu were incubated with B16F10 cells for 6 h. The intracellular fluorescence images and data were acquired with a confocal laser scanning microscopy (CLSM, Dragonfly 200, Andor, UK) and flow cytometry (CytoFLEX S, Beckman, USA).

2.2.5.   In vitro cell viability assay

B16F10 cells were incubated in fresh 1640 medium containing different concentrations of Cu^{2+}, Cu^{2+}+DSF, CLCu, and CLDCu for 24 h. The Cu^{2+}+DSF and CLDCu groups shared the same concentrations of DSF (0.38, 0.75, 1.5, 3.0, 4.5, and 6.0 µg/mL). A similar concentration of Cu^{2+} was given to all the groups (0.19, 0.38, 0.75, 1.5, 2.25, and 3.0 µg/mL). Finally, MTT assay was applied to measure the cell viability. The viability of HUVECs and BMDCs was determined in the similar method.

To measure the B16F10 cells viability in the presence of different inhibitors, ferroptosis inhibitor (ferrostatin-1, 10 mmol/L), necroptosis inhibitor (necrostatin-1, 20 mmol/L), oxidative stress inhibitor (n-acetylcysteine, 5 mmol/L), apoptosis inhibitor (Z-VAD-FMK, 30 mmol/L), and cuproptosis inhibitor (TTM, 20 mmol/L) were added and incubated with B16F10 cells overnight. Then, CLDCu (100 µg/mL) was injected into the culture medium of B16F10 cells. The cytotoxicity was then measured after 24 h.

2.2.6.   Evaluation of intracellular total ROS generation

For detecting total ROS generation, B16F10 cells were treated with PBS, Cu^{2+}, Cu^{2+}+DSF, CLCu, and CLDCu (50 µg/mL, the other groups were dosed with the same concentrations of Cu^{2+} or DSF) for 24 h. After that, the ROS generation was analyzed via flow cytometry. In addition, total ROS concentration was also detected by CLSM after being stained with DAPI for 20 min.

2.2.7.   Intracellular ATP detection

B16F10 cells were treated with PBS, Cu^{2+}, Cu^{2+}+DSF, CLCu, and CLDCu (50 µg/mL, the other groups were dosed with the same concentrations of Cu^{2+} or DSF) for 24 h. An ATP assay kit was applied to evaluate intracellular ATP contents after cells were harvested.

2.2.8.   Determination of intracellular Cu^+ content

The intracellular Cu^+ concentrations were evaluated using a Cu^+ colorimetric assay kit and Cu^+-responsive probe Coppersensor-1 (CS-1)[34]. B16F10 cells were incubated with Cu^{2+}, Cu^{2+}+DSF, CLCu, and CLDCu (50 µg/mL, the other groups were dosed with the same concentrations of Cu^{2+} or DSF) for 24 h. The Cu^+ amounts were determined using a Cu^+ colorimetric assay kit, as directed by the manufacturer. For Cu^+-responsive probe Coppersensor-1 (CS-1) to detect the concentrations of intracellular Cu^+, 5 µmol/L CS-1 was added for incubation with treated B16F10 cells. Data were acquired by flow cytometry.

2.2.9.   Western blot analysis of CLDCu-mediated cuproptosis

To perform Western blot analysis, B16F10 cells were subjected to various treatments: PBS, Cu^{2+}, Cu^{2+}+DSF, CLCu, and CLDCu (50 µg/mL, the other groups were dosed with the same concentrations of Cu^{2+} or DSF). A total of 20 µg protein/lane was separated using 7.5% or 12.5% SDS-PAGE. Next, the polyvinylidene fluoride (PVDF) membrane was incubated overnight with primary antibodies as follows: ATP7B polyclonal antibody (1:5000), DLAT polyclonal antibody (1:5000), Lipoic acid polyclonal antibody (1:6000), FDX1 monoclonal antibody (1:5000), and GAPDH monoclonal antibody (1:10,000). Subsequently, the membrane was incubated with secondary antibody. The protein expressions were evaluated by analyzing the gray levels.

2.2.10.   Evaluation of DLAT aggregation

PBS, Cu^{2+}, Cu^{2+}+DSF, CLCu, and CLDCu (50 µg/mL, the other groups were dosed with the same concentrations of Cu^{2+} and DSF) were respectively incubated with B16F10 cells for 24 h. The cells then were incubated with the DLAT antibody (1:100) at 4 °C overnight, stained with Alexa Fluor 488 anti-rabbit secondary antibody, Actin-tracker red, and DAPI and ultimately observed under CLSM. The immunofluorescence of ATP7B was performed following the same procedure with ATP7B antibody (1:100).

2.2.11.   Detection of immunogenic cell death (ICD)

First, the concentration of HMGB1 in cell culture supernatant was determined. Typically, different formulations were added to the B16F10 cells medium and incubated for 24 h. The HMGB1 content was detected by using ELISA kit. The contents of ATP in the supernatant were carried out in the same way. For immunofluorescence, the aforementioned treated cells were incubated with CRT antibody (1:100) at 4 °C overnight, and further stained with Alexa Flour 647-conjugated secondary antibody, and ultimately observed under CLSM.

2.2.12.   In vitro DCs maturation and cGAS−STING pathway activation

Bone marrow-derived dendritic cells (BMDCs) were used to evaluate whether CLDCu stimulates the maturation of DCs and activates the cGAS−STING pathway in DCs[35]. Specifically, 1×10^6 inactivated BMDCs were treated with different concentrations of CLDCu (0, 12.5, 25, 37.5, and 50 µg/mL) for 24 h. Then, BMDCs were stained with anti-CD11c-APC, anti-CD86-PE-Cy5.5, and anti-CD80-FITC according to the vendor's protocols, Then, BMDCs were detected by flow cytometry to investigate their maturation. Moreover, the expression of cGAS−STING pathway-related proteins, such as p-STING, p-IRF3, and p-TBK1 was analyzed using Western blotting.

2.2.13. Biodistribution

To investigate *in vivo* biodistribution patterns of CLDCu, the Cy5-substituted DSF was loaded in CLDCu, named Cy5-CLCu. Then, Cy5-CLCu (50 μL, 4 mg/mL) was inhaled into mice by microsprayer aerosolizer (MSA-250, PennCentury, USA). For comparison, Cy5-CLCu (50 μL, 4 mg/mL) was injected intravenously. At 1, 6, and 24 h after intravenous injection or inhalation of Cy5-CLCu, mice were sacrificed, and lungs and other major organs were collected for *ex vivo* imaging, and the lungs collected at 24 h were used for histological imaging.

2.2.14. In vivo anti-metastatic efficacy

Metastatic lung tumor model was established by intravenous injection of 3×10^5 B16F10 cells. After 7 days, mice were randomly divided into five groups, including 1: PBS (inh), 2: CLCu (inh), 3: CLDCu (i.v.), 4: CLDCu (inh), 5: CLDCu (inh) + aPD-L1 (i.v.). CLDCu (10 mg/kg) was inhaled three times every 7 days and aPD-L1 (3 mg/kg) was injected intravenously after inhalation of CLDCu for 24 h. The therapeutic results were mainly evaluated by the number of lung metastasis foci and survival rates of mice. The body weight was monitored every other day.

2.2.15. Immune effects

For analysis of DCs ($CD45^+CD11c^+CD80^+CD86^+$ DCs) maturation, lymph node cells were stained with anti-CD45-APC-Cy7, anti-CD11c-APC, anti-CD86-PE-Cy5.5, and anti-CD80-FITC. For the investigation of the level of $CD8^+$ T cells ($CD45^+CD3^+CD8a^+$ T cells), the single cell suspensions were stained with anti-CD45-APC-Cy7, anti-CD3-FITC, and anti-CD8a-PE for 30 min. For M1 macrophages and M2 macrophages ($CD45^+F4/80^+CD86^+CD206^-$ M1 macrophages, $CD45^+F4/80^+CD86^-CD206^+$ M2 macrophages) evaluation, the cell suspensions were labeled by anti-CD45-APC-Cy7, anti-F4/80-Brilliant violent 421 (BV421), anti-CD86-PE-Cy5.5, and anti-CD206-PE-Cy7. For the evaluation of immune-suppressive myeloid-derived suppressor cells (MDSCs) ($CD45^+CD11b^+Gr-1^+$ MDSCs) in metastatic lungs, anti-CD45-APC-Cy7, anti-CD11b-APC, and anti-Gr-1-PE were applied to stain the single cell suspensions for 30 min. For analysis of immune-suppressive cells regulatory T lymphocytes (Tregs) ($CD45^+CD4^+Foxp3^+$ Tregs), single-cell suspensions were firstly stained with anti-CD45-APC-Cy7 and anti-CD4-Percp/Cy5.5 for 30 min and further handled with True-Nuclear™ Perm buffer, and then stained with anti-Foxp3-Brilliant violent 421 (BV421) antibody for 60 min. The stained cells were analyzed by flowcytometry.

2.2.16. ELISA and mRNA analysis

The concentrations of IL-6, IL-12, TNF-α, and IFN-γ in lung metastatic sites were evaluated by ELISA kits. The qRT-PCR was applied to evaluate IFN-β and CXCL-10 expression. The following primers were used (5'→3'). M-GAPDH-S, GGTGAAGGTCGGTGTGAACG, M-GAPDH-A, CTCGCTCCT GGAAGATGGTG; M−IFN−β-S, CGTGGGAGATGTCCTCAA CT, M−IFN−β-A, TGAAGATCTCTGCTCGGACC; M-CXCL-10-S, GAGAGACATCCCGAGCCAAC, M-CXCL-10-A, TGGG CAGGATAGTCAACACG.

2.2.17. Statistical analysis

Software GraphPad Prism 8.0.2 was used for the data analysis. All quantitative data were presented as mean ± standard deviation (SD), and the differences between groups were assessed using two-sided Student *t*-test or one-way ANOVA with Tukey's *post hoc* test. Statistical differences were defined as ns means no significant difference, $^*P < 0.05$, $^{**}P < 0.01$, $^{***}P < 0.001$, $^{****}P < 0.0001$.

3. Results and discussion

3.1. Preparation, characterization, and cellular uptake of CLDCu

The construction process of CLDCu was illustrated in Fig. 1A. We first designed an amphiphilic conjugate, LMWH-TOS (LT) as previously described[32]. The LMWH (hydrophilic part) and TOS (hydrophobic part) were connected by esterification (Supporting Information Scheme S1). The structures of LT conjugate was characterized by ^{1}H-NMR and GPC (Supporting Information Fig. S1A−S1C). The peaks of LMWH (3.2−5.5 ppm) and TOS (1.0−3.0 ppm) in the LT ^{1}H NMR spectrum indicated the successful synthesis. The molecular weight (MW) of LT, as determined using GPC, was about 7.6 kDa. LT conjugate had a low critical micelle concentration of 0.06117 mg/mL (Supporting Information Fig. S2). Subsequently, DSF was encapsulated into the LT conjugate at a carrier/drug weight ratio as low as 10:1 by the single emulsification method, and the obtained nanodevice was denoted as LD (Supporting Information Fig. S3). To construct CLDCu, Cu^{2+} and chitosan were added to the emulsion of LD, and the Cu^{2+}-chitosan shell would rapidly form outside the LD core through electrostatic interactions. The morphology of LD and CLDCu were confirmed by transmission electron microscopy (TEM), and CLDCu exhibited a uniform structure (Fig. 2A). The hydration particle sizes of LD and CLDCu were 122.9 nm and 186.9 nm with PDIs of 0.234 and 0.105, respectively (Fig. 2B). Moreover, compared to LD, the zeta potential of CLDCu considerably increased to 4.5 from −25.9 mV (Fig. 2C). Furthermore, the elemental mapping images of N, S, and Cu elements confirmed the core−shell structure and successful preparation of CLDCu (Fig. 2D). And the ICP-MS results exhibited that the weight percentage of Cu and S (a characteristic element of DSF) in the prepared CLDCu was 2.97% (*w/w*) and 2.52% (*w/w*), respectively. In addition, CLDCu exhibited similar size and zeta potential within 7 days in PBS, indicating good stability of CLDCu (Supporting Information Fig. S4).

According to our design, CLDCu should possess tumor-specific biodegradability. Thus, we tested the pH-responsive properties of CLDCu. CLDCu exhibited weak release of Cu^{2+} in pH 7.4 (about 20%) and 6.8 (about 35%) PBS (Fig. 2E). Notably, after 24 h, CLDCu showed significantly accelerated Cu^{2+} release in pH 5.5 (about 90%). Moreover, as shown in Supporting Information Fig. S5A and S5B, CLDCu remained largely intact at pH 7.4 and 6.8 but dissociated under acidic condition during the 6 h incubation period. These results suggested that CLDCu possessed acid-responsive characteristics, possibly due to the breaking of coordination bond in Cu^{2+}-chitosan. As the aforementioned, the co-released Cu^{2+} and DSF could react with each other to generate CuET, which has characteristic absorption peaks at 263 and 429 nm[36]. Therefore, the UV−Vis−NIR absorbance values at 263 and 429 nm of CLDCu solutions were detected after dissolved in different pH PBS (7.4, 6.8, and 5.5). The absorption peak intensity of CLDCu at 263 and 429 nm gradually increased with time under pH = 5.5 condition, confirming the generation of CuET (Fig. 2F). Comparatively, under pH = 7.4 and 6.8 conditions, the absorption peak intensity
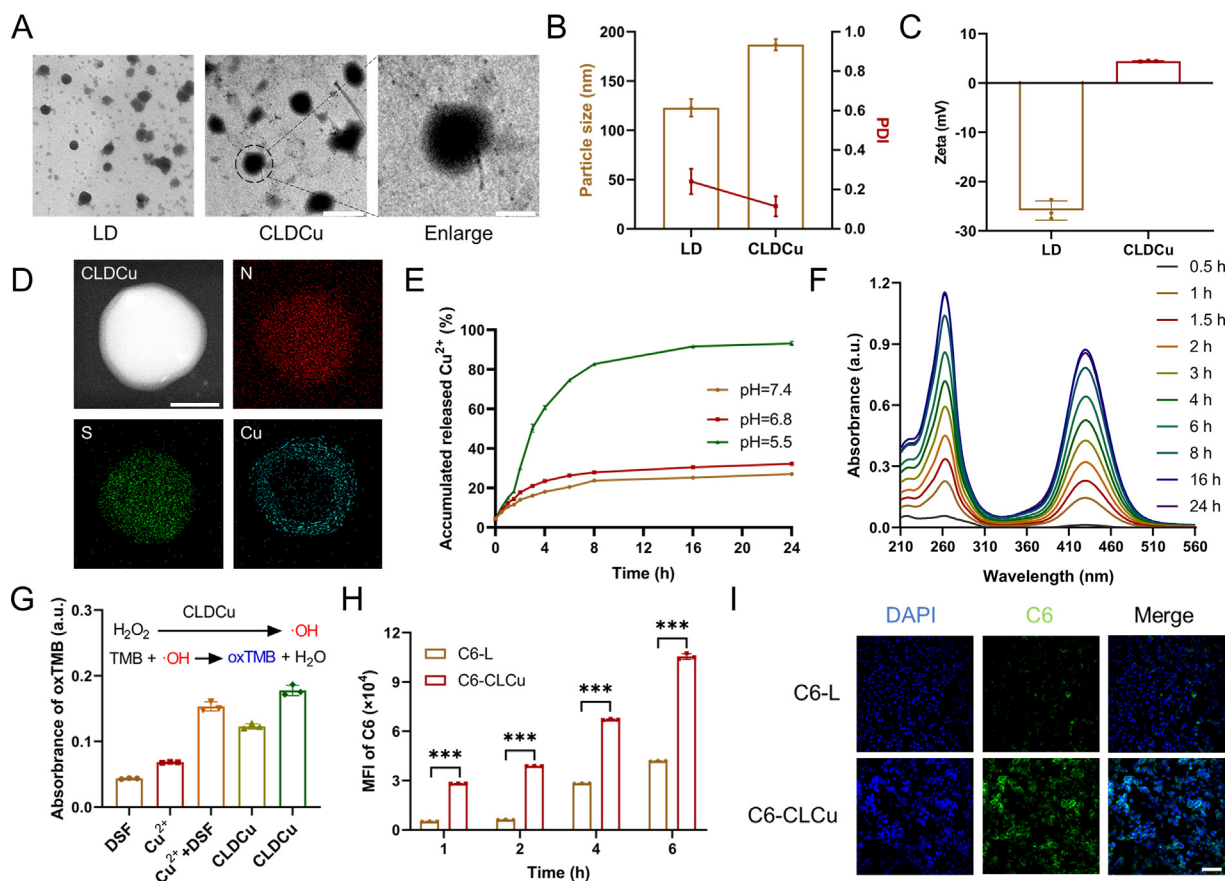
Figure 2 Preparation, characterization, and intracellular uptake of CLDCu. (A) LD and CLDCu (scale bar: 300 nm) and enlarged CLDCu TEM images (scale bar: 100 nm). (B) The hydrodynamic diameter and PDI of LD and CLDCu. (C) The zeta potentials of LD and CLDCu. (D) Element mapping of CLDCu. (E) Cumulative Cu^{2+} release from CLDCu at pH 7.4, 6.8, and 5.5. (F) UV−Vis absorbance spectra of CLDCu solution in the range of 210−560 nm after immersing in PBS (pH 5.5). (G) Absorbances of DSF, Cu^{2+}, Cu^{2+}+DSF, CLCu, and CLDCu after co-incubation with TMB and H_2O_2. (H) Mean fluorescence intensity (MFI) of fluorescence signals of B16F10 cells that incubated with C6-labeled LD or CLDCu for 1, 2, 4, and 6 h. (I) Representative CLSM pictures of B16F10 cells incubated with C6-L or C6-CLCu for 6 h. Cell nuclei were stained with DAPI (blue). Scale bar = 100 nm. Data are shown as mean ± SD (n = 3). ***P < 0.001.

of CuET decreased significantly at the same time point (Supporting Information Fig. S6A and S6B). Collectively, CLDCu showed acid-responsive degradation properties to release Cu^{2+} and DSF and subsequently generate CuET.

Next, we performed the functional characterizations of CLDCu in producing hydroxyl radical (OH). To verify the capability of CLDCu in generating ·OH, 3,3',5,5'-tetramethylbenzidine (TMB) was used (Fig. 2G)[33]. The Cu^{2+} and CLCu groups showed moderate absorption, indicating the generation of ·OH. Notably, the Cu^{2+}+DSF and CLDCu group has the increased absorption, which was ascribed to the CuET formation enhancing ·OH production. In addition, the ability of CLDCu to generate ·OH was detected in pH 7.4, 6.8, and 5.5 media. It was found that the trial performed in pH 5.5 condition exhibited a much stronger absorption at 652 nm than performed at pH 7.4 and 6.8, and the peak intensity at pH 5.5 notably increased with incubation time, indicating that CLDCu could efficiently generate ·OH in mildly acidic conditions (Supporting Information Fig. S7A and S7B).

To investigate the intracellular uptake of prepared nanoparticles, LD and CLDCu were labeled by coumarin 6 (C6, green), named C6-L and C6-CLCu. Obviously, after the Cu^{2+}-chitosan shell decoration, B16F10 cells incubated with C6-CLCu exhibited higher intracellular fluorescence signals than those of C6-L at 1, 2, 4, and 6 h (Fig. 2H). In addition, a similar result was found in the CLSM observation (Fig. 2I), where more green fluorescence signals in B16F10 cells treated with C6-CLCu group were observed at 6 h co-incubation. These results suggested that the better cellular uptake of the CLDCu was attributed to the modification of Cu^{2+}-chitosan shell.

3.2. The mechanism of CLDCu-mediated cuproptosis

As shown in Fig. 3A, the mechanism of CLDCu forming CuET involves the following two reactions: (1) Cu^{2+} and DSF released from CLDCu instantaneously react with each other to generate Cu^+ and bis(dialkylammonium)-tetrathiolanedication (Bitt-4^{2+}) intermediates. (2) Another DSF chelates with two Cu^+ to generate a Cu^{2+} and a CuET[36]. Subsequently, the ROS generation ability of CLDCu was evaluated by the 2',7'-dichlorofluorescein diacetate (DCFH-DA) (green). Fig. 3B indicated that the intracellular ROS levels were markedly increased in the CLCu and CLDCu groups and CLDCu was the most one, which was further supported by the CLSM images (Fig. 3C). These results demonstrated that

intracellular accumulated Cu^{2+} underwent a Fenton-like reaction to produce ROS, and the CuET formation could further enhance this process. Mitochondrial membrane potential protein (MMP) is known to be damaged by the overloaded ROS. As shown in Supporting Information Fig. S8, CLSM images exhibited a significant change in JC-1 fluorescence from red to green for the CLCu and CLDCu groups, demonstrated the disruption of MMP. Due to the damage of mitochondria membrane in cells, the ATP production was significantly inhibited. As expected, the ATP concentration of CLDCu-treated group was prominently reduced (Fig. 3D).

Subsequently, the intracellular Cu^+ contents after different treatments were measured by using the Cu^+ colorimetric assay kit and CS-1 (Cu^+ probe). Apparently, when compared with control group, CLCu and CLDCu groups displayed a remarkable increase of Cu^+ contents after 24 h incubation. Moreover, CLDCu group exhibited the highest Cu^+ concentration (Fig. 3E). A similar phenomenon was observed by using CS-1 probe (Supporting Information Fig. S9). These phenomena should be ascribed to the efficient cell endocytosis and subsequent formation of CuET, which generated large amounts of ROS to restrict ATP supply and further deactivate ATP7B protein, which is the major Cu^+ transmembrane transporter to expert Cu^+ out of cells. As displayed as Fig. 3F and Supporting Information Fig. S10, the expression of ATP7B was prominently down-regulated by CLDCu.

Then, we explored the cuproptosis-related protein expression and oligomerization of DLAT in B16F10 cells. The cells treated with Cu^{2+}+DSF moderately down-regulated Lip-DLAT, DLAT, and FDX1 proteins expression. The levels of Lip-DLAT, DLAT, and FDX1 in CLDCu group were 0.51-, 0.66-, and 0.66-fold of those in Cu^{2+}+DSF group (Fig. 3F and Supporting Information Fig. S11). Moreover, the expression of Lip-DLAT, DLAT, and FDX1 in CLDCu group were down-regulated than that in CLCu group, mainly due to preferable endocytosis of CLDCu and subsequent release of sufficient Cu^{2+} and DSF in the acidic condition that could chelate with each other to generate CuET for inhibiting ATP7B expression and convert to Cu^+, eventually triggering stronger cuproptosis. During cuproptosis, Cu^+ directly binds to Lip-DLAT, which causes DLAT aggregation. As displayed in Fig. 3G and Supporting Information Fig. S12, the Cu^{2+}-treated group showed almost no DLAT foci, while CLCu- and CLDCu-treated groups exhibited a higher degree of DLAT aggregation, especially CLDCu-treated group. These results demonstrated that our designed CLDCu system could effectively induce B16F10 cells cuproptosis.

Afterwards, the MTT assay was applied to test the viability of B16F10 cells after various treatments. The results exhibited that Cu^{2+} alone had no toxic effect on B16F10 cells. Yet, the Cu^{2+}+DSF, CLCu and CLDCu groups caused much more cell death, and CLDCu group was the most one, which is due to better cellular uptake and the massive formation of CuET and Cu^+ (Fig. 3H). Furthermore, the cytotoxicity of different nanoparticles towards human umbilical vein endothelial cells (HUVECs) was measured. Supporting Information Fig. S13 demonstrated that CLDCu had no effect on HUVECs cell viability. Moreover, to illuminate the mechanism of CLDCu-induced cell death, the necroptosis inhibitor (necrostatin-1, Nec-1), ferroptosis inhibitor (ferrostatin-1, Fer-1), oxidative stress inhibitor (n-acetylcysteine, NAC), apoptosis inhibitor (Z-VAD-FMK), and cuproptosis inhibitor (tetrathiomolybdate, TTM) were used. Fig. 3I indicated that the therapeutic activity of CLDCu was negligibly affected in the presence of Nec-1 and Fer-1, and slightly mitigated under

NAC and Z-VAD-FMK conditions, but obviously alleviated after addition of TTM, suggesting cuproptosis was mainly involved in the CLDCu-induced cell death pathway. In summary, CLDCu, on the one hand, provided a large amount of Cu^+ during the formation of CuET; on the other hand, deactivated the Cu^+ transmembrane transporter ATP7B to inhibit Cu^+ efflux, that together aggregated DLAT and decreased Fe−S cluster proteins, ultimately leading to enhanced cuproptosis (Fig. 3J).

3.3. Effect of CLDCu on DCs maturation in vitro

Previous studies have shown that cuproptosis may evoke ICD[37,38]. Considering the ability of CLDCu to trigger cuproptosis in tumor cells, we next investigated the capability of CLDCu to induce ICD[39]. To analyze the role of cuproptosis induced by CLDCu on ICD, we first evaluated the exposure of CRT after treatment with CLDCu. CLSM results demonstrated that CLDCu induced increased CRT exposure on the B16F10 cells surface (Fig. 4A). In addition, the ELISA results exhibited that the HMGB1 release content in CLDCu group was significantly higher than other groups (Fig. 4B). Moreover, the CLDCu group also showed the highest extracellular ATP content among all the groups (Fig. 4C). All these results indicated that CLDCu-triggered cuproptosis could evoke ICD.

To the best of our knowledge, DCs play an important role in inducing anti-tumor immune responses[40,41]. Emerging evidences have suggested that chitosan could stimulate DCs maturation[29,30]. Thus, we selected bone marrow-derived dendritic cells (BMDCs) as immature DCs to demonstrate that CLDCu has a similar stimulatory maturation effect on DCs. Before performing the immune activation-related assays, we evaluated the cytotoxicity of CLDCu in BMDCs. As shown in Supporting Information Fig. S14, CLDCu was highly safe to BMDCs. Next, to verify that CLDCu can stimulate DCs maturation, we cultured BMDCs with different concentrations of CLDCu for 24 h. As shown in Fig. 4D and E, enhanced expression of CD80 and CD86 on the surface of DCs was found, which proved that CLDCu could effectively promote DCs maturation. Besides, we cultured BMDCs with Cu^{2+}, Cu^{2+}+DSF, and CLCu for 24 h (Supporting Information Fig. S15A and S15B). It could be found that the CLCu group induced 30.79% mature DCs, which was 1.46- and 1.23-fold greater than the Cu^{2+} group (21.11%) and Cu^{2+}+DSF group (24.98%), respectively. Most importantly, after incubation with TTM (cuproptosis inhibitor), CLDCu exhibited attenuated effect in promoting DCs maturation.

We further tested the stimulatory ability of CLDCu on cGAS−STING signaling activation in BMDCs. The expression of cGAS−STING pathway-related proteins, such as phosphorylated STING (p-STING), phosphorylated IRF3 (p-IRF3), and phosphorylated TBK1 (p-TBK1) were evaluated by Western blotting (Fig. 4F and G). Exhilaratingly, the levels of p-STING, p-IRF3, and p-TBK1 in BMDCs were significantly increased after incubation with CLDCu. Moreover, as displayed in Fig. S15C and S15D, the TTM pretreated CLDCu group led to a down-regulation expression of p-STING, p-IRF3, and p-TBK1. These results verified that CLDCu-induced cuproptosis and released chitosan synergistically activated cGAS−STING pathway. Additionally, we explored the levels of IFN-β and C-X-C motif chemokine ligand 10 (CXCL-10)[42]. Results exhibited that the concentration of IFN-β was significantly up-regulated in BMDCs with CLDCu treatment, as was CXCL-10 (Fig. 4H and I). Moreover, increased secretion of interleukin-6 (IL-6) and TNF-α were observed in the CLDCu treatment group (Fig. 4J and K). In
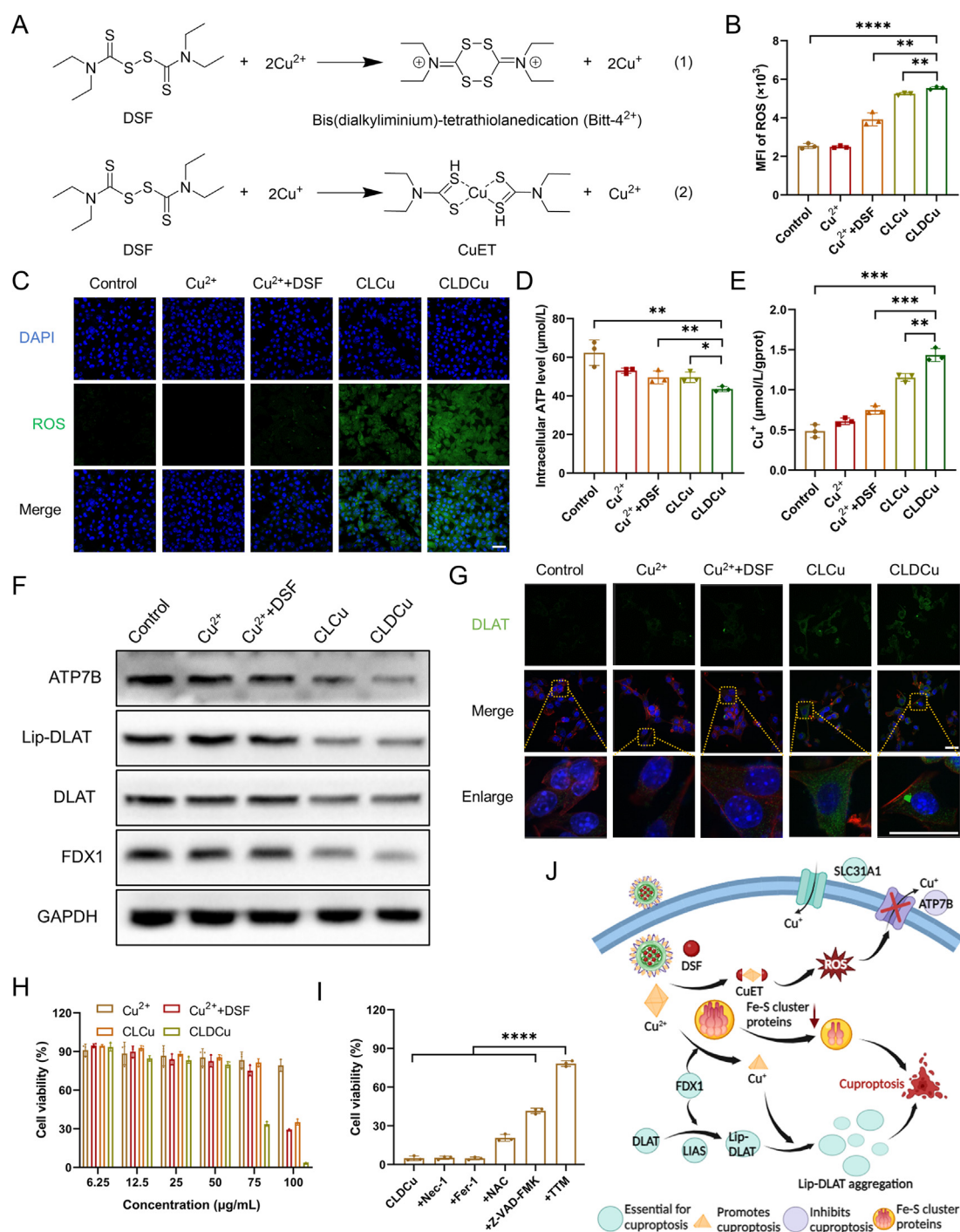
Figure 3 *In vitro* evaluation of CLDCu-mediated cuproptosis. (A) Mechanisms of DSF/Cu^{2+} reactions. (B) Quantitative analysis and (C) representative CLSM images of intracellular generated ROS. Scale bar $= 50$ μm. (D) Intracellular ATP levels of B16F10 cells after different treatments. (E) Intracellular Cu$^+$ contents after various treatments. (F) Western blot images of ATP7B, Lip-DLAT, DLAT, and FDX1 proteins in B16F10 cells. (G) DLAT immunofluorescence images of B16F10 cells. (blue, DAPI; red, Actin; green, DLAT). Scale bar $= 50$ μm. (H) Cell viability of B16F10 cells after each treatment. (I) Viability of B16F10 cells pretreated overnight with necrostatin-1 (Nec-1), ferrostatin-1 (Fer-1), nacetylcysteine (NAC), Z-VAD-FMK, tetrathiomolybdate (TTM), and then treated with CLDCu for 24 h. (J) Schematic illustration of CLDCu-mediated cuproptosis. Data are mean $\pm$ SD ($n = 3$). *$P < 0.05$, **$P < 0.01$, ***$P < 0.001$, ****$P < 0.0001$.

summary, these results suggested that CLDCu could efficiently evoke the antitumor immune responses by potentiating cGAS−STING activation, promoting DCs maturation, and stimulating proinflammatory cytokine release, thereby enhancing systemic antitumor immunity.

3.4. Inhalation administration and distribution behavior of CLDCu

A microsprayer aerosolizer (MSA-250, PennCentury, USA) was utilized for atomization experiments, which could atomize liquid
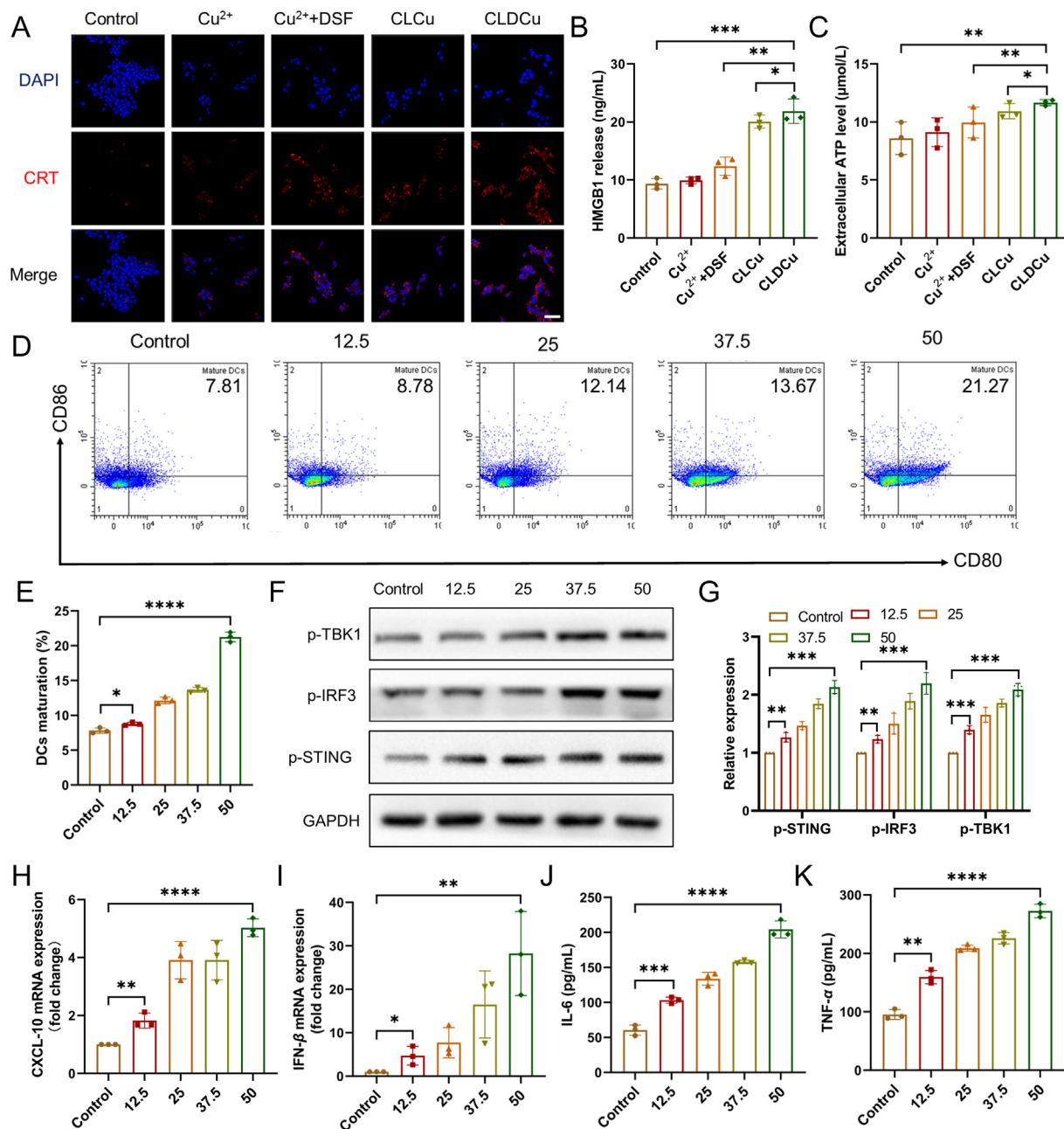
Figure 4 *In vitro* DCs maturation. (A) CLSM images showing CRT exposure in B16F10 cells after each treatment. Scale bar = 50 μm. The extracellular level of (B) HMGB1 and (C) ATP after different treatments for 24 h. (D, E) Quantification of the percentage of matured DCs after each treatment. (F) Western blot assay and (G) quantification of the expression of p-STING, p-IRF3, and p-TBK1 in DCs after incubation with different concentrations of CLDCu. The mRNA expression level of (H) CXCL-10 and (I) IFN-β in BMDCs treated by various concentrations of CLDCu. Quantitative analysis of (J) IL-6 and (K) TNF-α in the culture medium after treatment with CLDCu at different concentrations. Data are mean ± SD ($n = 3$). *$P < 0.05$, **$P < 0.01$, ***$P < 0.001$, ****$P < 0.0001$.

nanoparticles in a high-pressure way to achieve precise quantitative and high-concentration of direct pulmonary administration (Supporting Information Fig. S16A). First, we determined the effect of the atomization process on the physicochemical properties of CLDCu. As depicted in Fig. 5A, compared with CLDCu without atomization, the morphology and size of CLDCu after atomization did not change significantly. Furthermore, after atomization, the hydrodynamic size and zeta potential of CLDCu showed negligible changes (Fig. 5B and C). These findings

collectively demonstrated that the atomization process does not disrupt the structure of CLDCu and maintains high integrity.

Subsequently, we investigated the biodistribution of inhaled CLDCu in female C57BL/6J mice. Cy5 fluorescence dye instead of DSF was used in this experiment, named Cy5-CLCu (i.v.) and Cy5-CLCu (inh), respectively. After 1, 6, and 24 h inhalation or injection, mice were sacrificed, and major organs were dissected for *ex vivo* imaging. The intravenously injected Cy5-CLCu (Cy5-CLCu (i.v.)) was mainly manifested in the liver with little reaching the lungs. After

inhalation, the Cy5 fluorescence signal accumulation in lung sites significantly increased (about 56.5-fold) than the intravenous injection group at 1 h. Moreover, only inhalation of Cy5-CLCu (Cy5-CLCu (inh)) remained superior fluorescence in lung tissues after 24 h, which demonstrated the excellent lung retention properties of inhaled Cy5-CLCu (Fig. 5D and E). The brightest fluorescence signal of lung sites after Cy5-CLCu inhalation for 24 h also indicated the excellent lung accumulation and retention properties (Fig. 5F). To quantitatively analyze the distribution behavior of CLDCu, we further detected the Cu content in lung and other major organs (heart, live, spleen, and kidney) by ICP-MS at 1, 6, and 24 h. Results presented in Fig. S16B indicated more Cu accumulation within lung tissues after inhalation of CLDCu compared to other major organs. Next, to evaluate *in vivo* pharmacokinetics, the plasma levels of Cy5 were measured after inhalation or intravenous injection of Cy5-CLCu. The Cy5 percentage content in the blood of the mice in the inhalation group was $7.04 \pm 0.83\%$ after 24 h, while the Cy5 percentage content in the injection group was undetectable after 8 h (Fig. S16C).

3.5. *In vivo therapeutic efficacy of inhaled CLDCu combined with aPD-L1*

Subsequently, we evaluated the anti-metastatic efficacy of CLDCu combined with PD-L1 checkpoint blockade *in vivo*. Mice bearing B16F10 melanoma lung metastasis were selected as a lung metastasis model[23]. Mice were randomly divided into five groups: 1: PBS (inh), 2: CLCu (inh), 3: CLDCu (i.v.), 4: CLDCu (inh), 5: CLDCu (inh) + aPD-L1 (i.v.) (i.v. stands for intravenous injection and inh refers to inhalation). As shown in Fig. 6A, different materials were injected intravenously or inhaled for three times every 7 days, and aPD-L1 antibodies (3 mg/kg) were injected together after inhalation of CLDCu for 24 h.

As shown in Fig. 6B and Supporting Information Fig. S17, numerous metastatic nodules were seen in the lungs of PBS-treated mice. Moreover, compared with CLDCu (i.v.) group, CLDCu (inh) treated group showed a substantial reduction in lung surface nodules, especially in combination with aPD-L1 (i.v.). In addition, the stable body weight curve exhibited by each treatment group during the treatment period demonstrated the biosafety of the prepared CLDCu *in vivo* (Fig. 6C). Then, we evaluated the efficacy of CLDCu (inh) combined with aPD-L1 (i.v.) on prolonging the survival of lung metastasis model (Fig. 6D). During the 60-day observation period, the overall survival of mice in the CLDCu (inh) + aPD-L1 (i.v.) group was significantly prolonged.

Moreover, haematoxylin and eosin (H&E) staining showed plentiful lung metastatic nodules in the PBS (i.v.)- and CLDCu (i.v.)-treated groups, while extremely few metastatic lesions were observed in CLDCu (inh)- and CLDCu (inh) + aPD-L1 (i.v.)-treated groups (Fig. 6E). To further elucidate the anti-metastatic mechanism of CLDCu *in vivo*, DLAT expression in lung tissues was examined by immunofluorescence assay. More pronounced aggregation of DLAT was observed in CLDCu (inh) and CLDCu (inh) + aPD-L1 (i.v.) treated group, verifying the presence of cuproptosis *in vivo* (Fig. 6E). In summary, the combination therapy of CLDCu (inh) + aPD-L1 (i.v.) could achieve highly effective anti-metastatic effects.

3.6. *Anti-metastatic immune response elicited by CLDCu combined with aPD-L1*

Firstly, we explored the effects of inhalation of CLDCu on the expression of CRT (a biomarker of ICD) in lung metastasis sections by immunofluorescence staining. Results showed significantly amplified CRT exposure in CLDCu (inh) and CLDCu
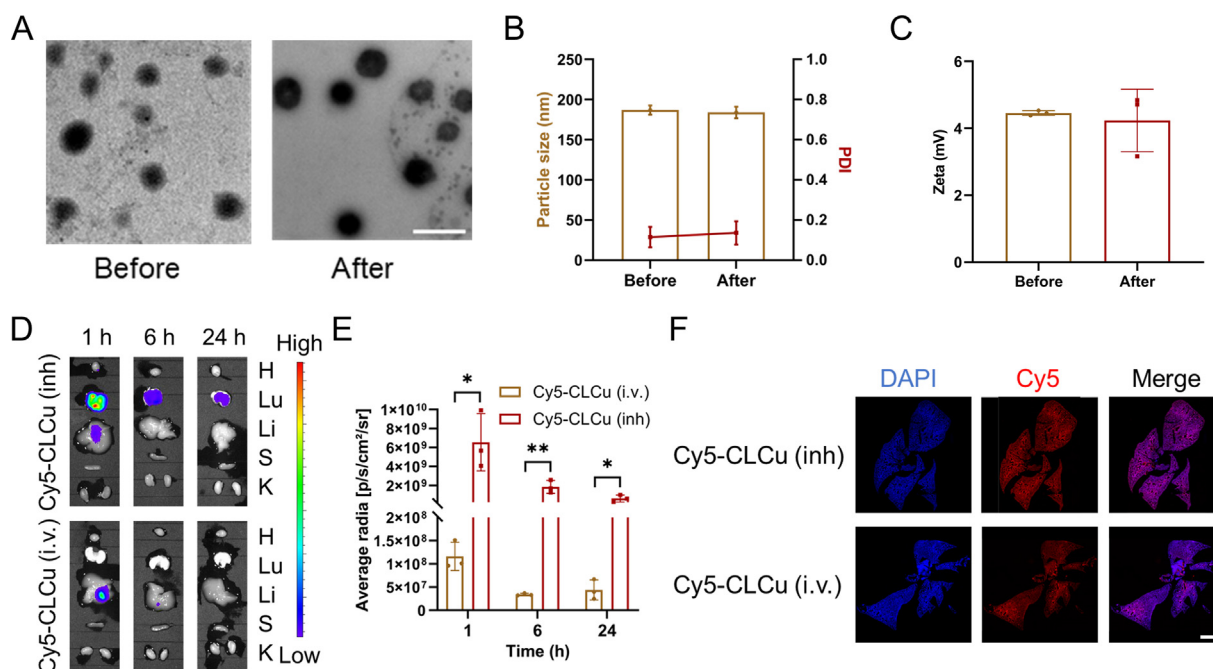

Figure 5 *In vivo* distribution of CLDCu after different administration. (A) TEM image of CLDCu solutions before and after atomization (scale bar = 300 nm). (B) The hydrodynamic diameter and PDI of CLDCu before and after atomization. (C) The zeta potential of CLDCu before and after atomization. (D) *Ex vivo* fluorescence images of lung and other major organs at different time intervals after inhalation or intravenous injection of Cy5-CLCu (H, heart; Lu, lung; Li, liver; S, spleen; K, kidney). (E) Quantitative analysis of Cy5-CLCu in lung tissues at different time points. (F) Representative fluorescence images of lung sections after 24 h of various administration (scale bar = 1 mm). i.v. stands for intravenous injection, and inh refers to inhalation. Data are mean ± SD (*n* = 3). *P < 0.05, **P < 0.01.

(inh) + aPD-L1 (i.v.) groups, that demonstrating the most effective ICD induced by inhalation of CLDCu (Fig. 7A). Moreover, the expression of p-STING, p-TBK1, and p-IRF3 in lung metastatic tissues were investigated (Fig. 7A, and Supporting Information Fig. S18A and S18B). Obvious red fluorescence signals of p-STING, p-TBK1, and p-IRF3 were observed in lung metastatic tissues slices of the CLDCu (inh) and CLDCu (inh) + aPD-L1 (i.v.) groups. In addition, the mRNA expression of CXCL-10 and IFN-β in lung metastatic sites of mice treated with CLDCu (inh) and CLDCu (inh) + aPD-L1 (i.v.) was significantly increased compared with other groups, demonstrating that the cGAS−STING pathway was successfully activated by inhalation of CLDCu (Supporting Information Fig. S19A and S19B). Subsequently, the DCs maturation in tumor-draining lymph nodes was quantified *via* flow cytometry. As displayed in Fig. 7B and Supporting Information Fig. S20A, the matured DC cells (CD80$^+$CD86$^+$) in CLDCu (inh)-treated mice was 2.06 times higher than that in PBS-treated mice (CLDCu (inh) *vs.* PBS = 2.21% *vs.* 1.08%). Besides, the CLDCu (inh) + aPD-L1 (i.v.) group with the highest level (2.58%) indicated that CLDCu (inh) and aPD-L1 synergistically induced DCs maturation. In addition, CD8$^+$ T cell infiltration in lung metastatic tissues was further analyzed. Flow cytometry results observed an enhanced CD8$^+$ T cells activation (7.50%, CD3$^+$CD8$^+$ T cells) in CLDCu (inh) + aPD-L1 (i.v.) treated group, which was 1.81, 1.38, 1.17,

and 1.10 times greater than the PBS (4.14%), CLCu (inh) (5.42%), CLDCu (i.v.) (6.39%), and CLDCu (inh) groups (6.84%), respectively (Fig. 7C and Fig. S20B).

It is reported that TAM are classified into two types in tumors: M1-type (inhibit tumor growth) and M2-type (inhibit T cells proliferation)[43,44]. As shown in Fig. 7D and Fig. S20C, the M1 to M2 ratio in CLDCu (inh) + aPD-L1 (i.v.) group (33.5%) was 2.86-, 1.98-, 1.29-, and 1.04-fold higher than the PBS, CLCu (inh), CLDCu (i.v.), and CLDCu (inh) groups, respectively. It is reported that Tregs (CD3$^+$CD4$^+$Foxp3$^+$) can suppress antitumor immune activation[45]. The flow cytometry results demonstrated that CLDCu (inh) + aPD-L1 (i.v.) treatment effectively decreased the percentage of Tregs (CLDCu (inh) + aPD-L1 (i.v.) *vs.* PBS = 22.2% *vs.* 42.3%, Fig. 7E and Fig. S20D). In addition, the CLDCu (inh) + aPD-L1 (i.v.) treatment also obviously reduced the intratumoral frequency of MDSCs (CD11b$^+$Gr-1$^+$) (Fig. 7F and Fig. S20E), a subset of immunosuppressive immature myeloid cells[46]. Collectively, these results demonstrated that the CLDCu (inh) + aPD-L1 (i.v.) group could effectively trigger immune responses and alleviate immune suppression.

In addition, the secretions of proinflammatory cytokines such as IL-6, IL-12, interferon-γ (IFN-γ), and TNF-α in lung metastasis tissues were analyzed *via* ELISA. The secretion of IL-6 was highest after CLDCu (inh) + aPD-L1 (i.v.) treatment, showing a 1.92-fold increase compared with PBS group (Fig. 7G). Similarly, the
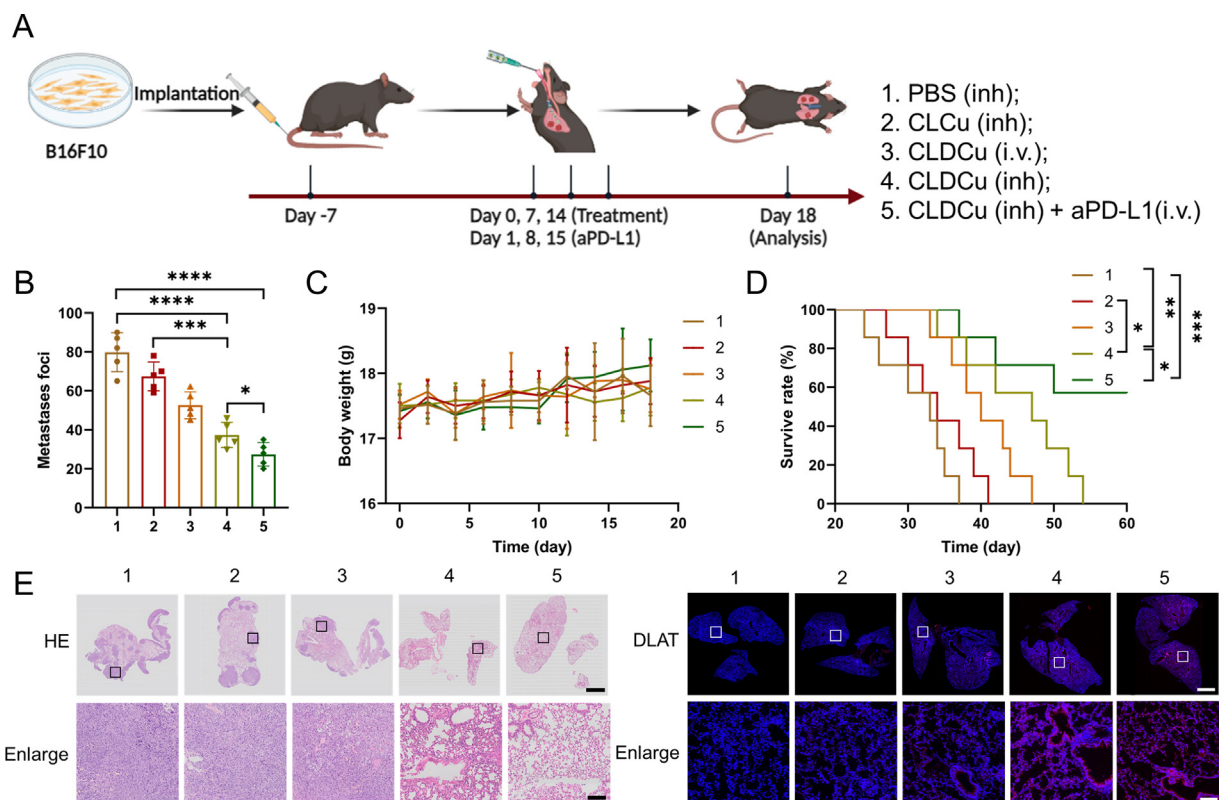

Figure 6 Therapeutic efficacy of CLDCu inhalation synergized with aPD-L1 in lung metastasis model. (A) The treatment schedule for evaluation of combined CLDCu and aPD-L1. (B) Number statistics of metastasis foci in lungs ($n = 5$). (C) The body weight of mice in different treatment groups changed during the treatment ($n = 5$). (D) The survival curves of mice in different treatment groups within 60 days and statistically analyzed by log-rank test ($n = 7$). (E) H&E images and DLAT immunofluorescence staining of lung sections (scale bar: 1 mm) and magnified images (scale bar: 100 μm). 1: PBS (inh), 2: CLCu (inh), 3: CLDCu (i.v.), 4: CLDCu (inh), 5: CLDCu (inh) + aPD-L1 (i.v.). Data are mean ± SD. *$P < 0.05$, **$P < 0.01$, ***$P < 0.001$, ****$P < 0.0001$.
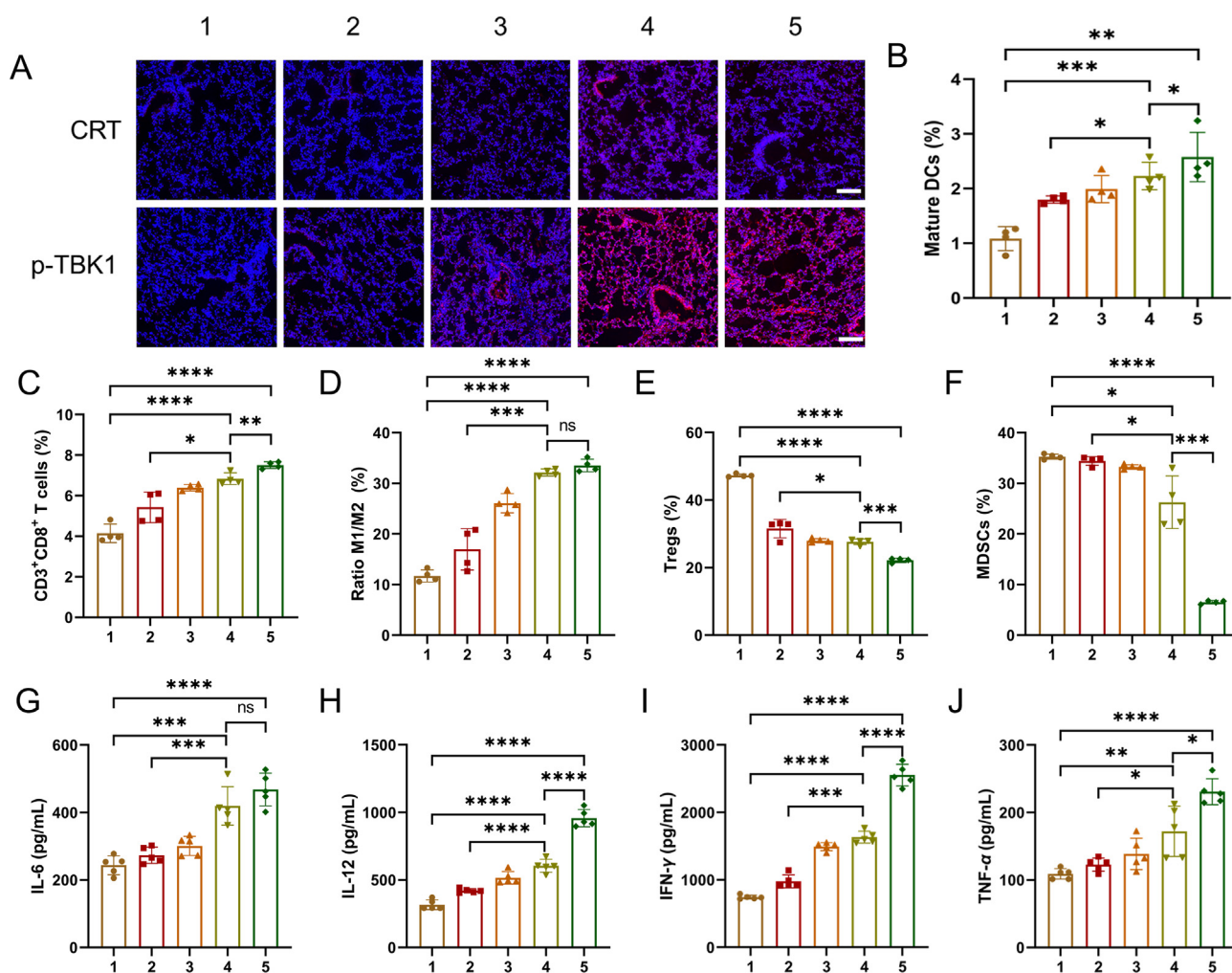
Figure 7 *In vivo* robust anti-metastatic immune response elicited by inhalation of CLDCu combined with aPD-L1. (A) Representative immunofluorescence images of lung tissues stained by CRT and p-TBK1 assay after different treatments. Scale bar = 100 μm. (B) The levels of matured DCs in lymph nodes ($n = 4$). (C) Relative ratio of CD8$^+$ T cells in lung metastatic tissues ($n = 4$). (D) The ratios of M1/M2 macrophages in lung metastatic tissues ($n = 4$). (E) Flow cytometry analysis of Tregs ($n = 4$). (F) Relative ratio of MDSCs cells in lung metastatic tissues ($n = 4$). Cytokine contents of (G) IL-6, (H) IL-12, (I) IFN-γ, and (J) TNF-α in lung metastatic tissues after treatment of each formulation ($n = 5$). 1: PBS (inh), 2: CLCu (inh), 3: CLDCu (i.v.), 4: CLDCu (inh), 5: CLDCu (inh) + aPD-L1 (i.v.). Data are mean ± SD. ns means no significant difference, *$P < 0.05$, **$P < 0.01$, ***$P < 0.001$, ****$P < 0.0001$.

secretion of IL-12 (Fig. 7H), IFN-γ (Fig. 7I), and TNF-α (Fig. 7J) also showed a substantial increase in CLDCu (inh) + aPD-L1 (i.v.) group. Taken together, these results illuminated that the CLDCu with amplified cuproptosis and cGAS−STING activation combined with aPD-L1 could elicit strong anticancer immune response and remodel immuno-microenvironment.

3.7. Biocompatibility of CLDCu

Next, the biosafety of CLDCu were explored. To this end, PBS and CLDCu (10 mg/kg) were inhaled or injected into healthy female C57BL/6J mice for three times every 7 days. The H&E staining of lungs and other normal organs including heart, liver, spleen, and kidney collected on Day 18 proved there were no apparent pathological abnormalities observed in mice after various treatments (Supporting Information Fig. S21A). In addition, the hemolysis assay showed that CLDCu had only a slight influence on blood erythrocytes (Fig. S21B). Moreover, all of the tested liver

function indexes (aspartate aminotransferase (AST) and alanine aminotransferase (ALT)) and kidney function indexes (blood urea nitrogen (BUN) and creatinine (CRE)) showed little variation between the groups (Fig. S21C−S21F).

Subsequently, the cytotoxicity of CLDCu in alveolar epithelial cells (AECs) was examined. As shown in Supporting Information Fig. S22A, CLDCu did not exhibit cytotoxic effect, suggesting an excellent safety profile in normal lung cells. Furthermore, various lungs function tests were carried out in healthy mice on Days 3, 10, and 17. Our results showed that multiple pulmonary function (total lung capacity (TLC), forced vital capacity (FVC), functional residual capacity (FRC), peak expiratory flow (PEF), and forced expiratory volume in 50 ms (FEV50)) in the lungs were downregulated in the acute stage (Day 3) after inhalation of CLDCu (Fig. S22B−S22F). However, the levels of lung function indicators on Day 10 and 17 returned to normal levels. Overall, these above results demonstrated that CLDCu possessed good biocompatibility.

4. Conclusions

In summary, we have developed an inhalable nanodevice CLDCu with potentiated cuproptosis and cGAS−STING activation for efficient lung metastasis immunotherapy. CLDCu consisted of a Cu^{2+}-chitosan shell and LT core with DSF loading. CLDCu exhibited excellent accumulation in lung tissues by inhalation administration, and with negligible adverse effects. Upon reaching lung metastatic tissues, the Cu^{2+}-chitosan shell enabled the enhanced tumor cellular uptake. After internalization, CLDCu was degraded in the acidic microenvironment, releasing Cu^{2+} and DSF, leading to *in situ* chelation reaction to generate CuET for down-regulating Cu^+ efflux protein ATP7B expressions and Cu^+ for directly binding to Lip-DLAT aggregation and destabilizing Fe−S cluster proteins, eventually inducing tumor cells cuproptosis, as well as releasing amounts of DAMPs. Moreover, chitosan enhanced the cuproptosis-mediated antitumor response *via* amplifying the cGAS−STING pathway activation in the DCs. *In vivo*, inhalation of CLDCu exhibited strong antitumor responses: (1) the loaded Cu^{2+} and DSF could accurately induce tumor cells cuproptosis. (2) Chitosan served as an immunomodulator combined with CLDCu-mediated cuproptosis activated the cGAS−STING pathway. (3) The treatment finally stimulated DCs maturation, promoted $CD8^+$ T cells infiltration, and remodeled immunosuppressive TME. Moreover, CLDCu collaborated with aPD-L1 could provoke more powerful antitumor immunity to inhibit the occurrence of lung metastasis. Overall, our study provided an innovative strategy to elicit antitumor response through inhalation of nanoplatform with enhanced cuproptosis and cGAS−STING activation.

Acknowledgments

Author contributions

Zhongxi Zhao and Chongzheng Yan conceived and administered the project. Chongzheng Yan, Huaiyou Lv, Yafei Feng, and Yuhan Li conducted the investigation. Chongzheng Yan performed experiments. Zhongxi Zhao applied for the funding. Chongzheng Yan wrote the manuscript. Zhongxi Zhao supervised the project. All of the authors have read and approved the final manuscript.

Conflicts of interest

The authors declare no conflicts of interest.

Appendix A. Supporting information

Supporting information to this article can be found online at https://doi.org/10.1016/j.apsb.2024.04.028.

References

1. Nicholson AG, Scagliotti G, Tsao MS, Yatabe Y, Travis WD. WHO classification of lung cancer: a globally applicable and molecular biomarker-relevant classification. *J Thorac Oncol 2022* 2021;**17**: e80−3.

2. Malvezzi M, Santucci C, Boffetta P, Collatuzzo G, Levi F, La Vecchia C, et al. European cancer mortality predictions for the year 2023 with focus on lung cancer. *Ann Oncol* 2023;**34**:410−9.

3. Rezaie J, Ahmadi M, Ravanbakhsh R, Mojarad B, Mahbubfam S, Shaban SA, et al. Tumor-derived extracellular vesicles: the metastatic organotropism drivers. *Life Sci* 2022;**289**:120216.

4. Fu AK, Yao BQ, Dong TT, Chen YY, Yao J, Liu Y, et al. Tumor-resident intracellular microbiota promotes metastatic colonization in breast cancer. *Cell* 2022;**185**:1356−72.

5. Ding CL, Shrestha R, Zhu XJ, Geller AE, Wu SZ, Woeste MR, et al. Inducing trained immunity in pro-metastatic macrophages to control tumor metastasis. *Nat Immunol* 2023;**24**:239−54.

6. Xu JB, Cao J, Xia J, Zhu Y, He Y, Cao MG, et al. Breast metastatic tumors in lung can be substituted by lung-derived malignant cells transformed by alternative splicing H19 lncRNA. *Breast Cancer Res* 2023;**25**:59.

7. Wu MM, Liang YF, Zhang X. Changes in pulmonary microenvironment aids lung metastasis of breast cancer. *Front Oncol* 2022;**12**: 860932.

8. Li W, Liu JB, Hou LK, Yu F, Zhang J, Wu W, et al. Liquid biopsy in lung cancer: significance in diagnostics, prediction, and treatment monitoring. *Mol Cancer* 2022;**21**:25.

9. Que ZJ, Tian JH. New strategy for antimetastatic treatment of lung cancer: a hypothesis based on circulating tumour cells. *Cancer Cell Int* 2022;**22**:356.

10. Tian H, Bai GY, Yang ZL, Chen P, Xu JC, Liu TJ, et al. Multiple primary lung cancer: updates of clinical management and genomic features. *Front Oncol* 2023;**13**:1034752.

11. Brahmer JR, Lee JS, Ciuleanu TE, Bernabe CR, Nishio M, Urban L, et al. Five-year survival outcomes with nivolumab plus ipilimumab *versus* chemotherapy as first-line treatment for metastatic non-small-cell lung cancer in checkmate 227. *J Clin Oncol* 2023;**41**:1200−12.

12. Tsvetkov P, Coy S, Petrova B, Dreishpoon M, Verma A, Abdusamad M, et al. Copper induces cell death by targeting lipoylated TCA cycle proteins. *Science* 2022;**375**:1254−61.

13. Tong XH, Tang R, Xiao MM, Xu J, Wang W, Zhang B, et al. Targeting cell death pathways for cancer therapy: recent developments in necroptosis, pyroptosis, ferroptosis, and cuproptosis research. *J Hematol Oncol* 2022;**15**:174.

14. Chen MX, Huang ZQ, Xia M, Ding YQ, Shan T, Guan ZL, et al. Glutathione-responsive copper-disulfiram nanoparticles for enhanced tumor chemotherapy. *J Control Release* 2022;**341**:351−63.

15. Roelofsen H, Wolters H, Van Luyn MJ, Miura N, Kuipers F, Vonk RJ. Copper-induced apical trafficking of ATP7B in polarized hepatoma cells provides a mechanism for biliary copper excretion. *Gastroenterology* 2000;**119**:782−93.

16. Cater MA, La Fontaine S, Shield K, Deal Y, Mercer JF. ATP7B mediates vesicular sequestration of copper: insight into biliary copper excretion. *Gastroenterology* 2006;**130**:493−506.

17. Wu WC, Yu LD, Jiang QZ, Huo MF, Lin H, Wang LY, et al. Enhanced tumor-specific disulfiram chemotherapy by *in situ* Cu^{2+} chelation-initiated nontoxicity-to-toxicity transition. *J Am Chem Soc* 2019; **141**:11531−9.

18. Zhou J, Yu Q, Song J, Li S, Li XL, Kang BK, et al. Photothermally triggered copper payload release for cuproptosis-promoted cancer synergistic therapy. *Angew Chem Int Ed Engl* 2023;**62**:e202213922.

19. Falls-Hubert KC, Butler AL, Gui K, Anderson M, Li MS, Stolwijk JM, et al. Disulfiram causes selective hypoxic cancer cell toxicity and radio-chemosensitization *via* redox cycling of copper. *Free Radic Biol Med* 2020;**150**:1−11.

20. Fu FQ, Wang WH, Wu LJ, Wang WH, Huang ZW, Huang Y, et al. Inhalable biomineralized liposomes for cyclic Ca^{2+}-burst-centered endoplasmic reticulum stress enhanced lung cancer ferroptosis therapy. *ACS Nano* 2023;**17**:5486−502.

21. Liu Y, Crowe WN, Wang LL, Lu Y, Petty WJ, Habib AA, et al. An inhalable nanoparticulate STING agonist synergizes with radiotherapy to confer long-term control of lung metastases. *Nat Commun* 2019;**10**:5108.

22. Zoulikha M, Xiao QQ, Boafo GF, Sallam MA, Chen ZJ, He W. Pulmonary delivery of siRNA against acute lung injury/acute respiratory distress syndrome. *Acta Pharm Sin B* 2022;**12**:600−20.

23. Jin QY, Zhu WJ, Zhu JF, Zhu JJ, Shen JJ, Liu Z, et al. Nanoparticle-mediated delivery of inhaled immunotherapeutics for treating lung metastasis. *Adv Mater* 2021;**33**:e2007557.

24. Jin XK, Liang JL, Zhang SM, Huang QX, Zhang SK, Liu CJ, et al. Orchestrated copper-based nanoreactor for remodeling tumor microenvironment to amplify cuproptosis-mediated anti- tumor immunity in colorectal cancer. *Mater Today* 2023;**68**:108−24.

25. Huang QX, Liang JL, Chen QW, Jin XK, Niu MT, Dong CY, et al. Metal-organic framework nanoagent induces cuproptosis for effective immunotherapy of malignant glioblastoma. *Nano Today* 2023;**51**:101911.

26. Tian HL, Duan JF, Li BW, Qin SY, Nice EC, Zhang W, et al. Clinical chemotherapeutic agent coordinated copper-based nanoadjuvants for efficiently sensitizing cancer chemo-immunotherapy by cuproptosis-mediated mitochondrial metabolic reprogramming. *Adv Funct Mater* 2023;**12**:2306584.

27. Wang YJ, Gong F, Han ZH, Lei HL, Zhou YK, Cheng SN, et al. Oxygen-deficient molybdenum oxide nanosensitizers for ultrasound-enhanced cancer metalloimmunotherapy. *Angew Chem Int Ed Engl* 2023;**62**:e202215467.

28. Chen Q, Li CY, Wang QB. Multifunctional nano-biomaterials for cancer therapy *via* inducing enhanced immunogenic cell death. *Small Methods* 2023;**7**:2201457.

29. Carroll EC, Jin L, Mori A, Munoz-Wolf N, Oleszycka E, Moran HB, et al. The vaccine adjuvant chitosan promotes cellular immunity *via* DNA sensor cGAS−STING-dependent induction of type I interferons. *Immunity* 2016;**44**:597−608.

30. Turley JL, Moran HB, Mcentee CP, Grady KO, Munoz-Wolf N, Jin L, et al. Chitin-derived polymer deacetylation regulates mitochondrial reactive oxygen species dependent cGAS−STING and NLRP3 inflammasome activation. *Biomaterials* 2021;**275**:120961.

31. Wu ML, Zhang X, Zhao Y, Yang CP, Jing SS, Wu QS, et al. A high-performance hydroxide exchange membrane enabled by Cu^{2+}-cross-linked chitosan. *Nat Nanotechnol* 2022;**17**:629−36.

32. Long Y, Lu ZZ, Mei L, Li M, Ren KB, Wang XH, et al. Enhanced melanoma-targeted therapy by "fru-blocked" phenyboronic acid-modified multiphase antimetastatic micellar nanoparticles. *Adv Sci* 2018;**5**:1800229.

33. Xu WJ, Qian JM, Hou GH, Wang TB, Wang JL, Wang YP, et al. A hollow amorphous bimetal organic framework for synergistic cuproptosis/ferroptosis/apoptosis anticancer therapy *via* disrupting intracellular redox homeostasis and copper/iron metabolisms. *Adv Funct Mater* 2022;**32**:2205013.

34. Zeng L, Miller EW, Pralle A, Isacoff EY, Chang CJ. A selective turn-on fluorescent sensor for imaging copper in living cells. *J Am Chem Soc* 2006;**128**:10−1.

35. Tian H, Wang GH, Sang W, Xie LS, Zhang Z, Li WX, et al. Manganese-phenolic nanoadjuvant combines sonodynamic therapy with cGAS−STING activation for enhanced cancer immunotherapy. *Nano Today* 2022;**43**:101405.

36. Wu WC, Yu LD, Pu YY, Yao HL, Chen Y, Shi JL. Copper-enriched prussian blue nanomedicine for *in situ* disulfiram toxification and photothermal antitumor amplification. *Adv Mater* 2020;**32**:2000542.

37. Li B, Hao GY, Sun B, Gu Z, Xu ZP. Engineering a therapy-induced "immunogenic cancer cell death" amplifier to boost systemic tumor elimination. *Adv Funct Mater* 2020;**30**:1909745.

38. Li QY, Chen C, Kong JX, Li L, Li JL, Huang Y. Stimuli-responsive nano vehicle enhances cancer immunotherapy by coordinating mitochondria-targeted immunogenic cell death and PD-L1 blockade. *Acta Pharm Sin B* 2022;**12**:2533−49.

39. Zhong HH, Chen GJ, Li T, Huang JS, Lin MZ, Li B, et al. Nanodrug augmenting antitumor immunity for enhanced TNBC therapy *via* pyroptosis and cGAS−STING activation. *Nano Lett* 2023;**23**:5083−91.

40. Yi YF, Yu M, Feng C, Hao HS, Zeng WW, Lin CC, et al. Transforming "cold" tumors into "hot" ones *via* tumor-microenvironment-responsive siRNA micelleplexes for enhanced immunotherapy. *Matter* 2022;**5**: 2285−305.

41. Xu JL, Ma QL, Zhang Y, Fei ZY, Sun YF, Fan Q, et al. Yeast-derived nanoparticles remodel the immunosuppressive microenvironment in tumor and tumor-draining lymph nodes to suppress tumor growth. *Nat Commun* 2022;**13**:110.

42. Huang Y, Qin G, Cui TT, Zhao CQ, Ren JS, Qu XG. A bimetallic nanoplatform for STING activation and CRISPR/Cas mediated depletion of the methionine transporter in cancer cells restores antitumor immune responses. *Nat Commun* 2023;**14**:4617.

43. Kobatake K, Ikeda KI, Nakata Y, Yamasaki N, Ueda T, Kanai A, et al. Kdm6a deficiency activates inflammatory pathways, promotes M2 macrophage polarization, and causes bladder cancer in cooperation with p53 dysfunction. *Clin Cancer Res* 2020;**26**:2065−79.

44. Mantovani A, Allavena P, Marchesi F, Garlanda C. Macrophages as tools and targets in cancer therapy. *Nat Rev Drug Discov* 2022;**21**: 799−820.

45. Grover A, Sanseviero E, Timosenko E, Gabrilovich DI. Myeloid-derived suppressor cells: a propitious road to clinic. *Cancer Discov* 2021;**11**:2693−706.

46. Hegde S, Leader AM, Merad M. MDSC: markers, development, states, and unaddressed complexity. *Immunity* 2021;**54**:875−84.